Geomechanics and Engineering, *Vol. 25, No. 3 (2021) 179-194*
DOI: https://doi.org/10.12989/gae.2021.25.3.179

Study on bearing characteristic of rock mass with different structures: Physical modeling

Zhenlong Zhao[1], Hongwen Jing[*1], Xinshuai Shi[1,2], Lijun Yang[1], Qian Yin[1] and Yuan Gao[**1,3]

[1]*State Key Laboratory for Geomechanics and Deep Underground Engineering, China University of Mining and Technology, Xuzhou 221116, P.R. China*
[2]*Graduate School of Engineering, Nagasaki University, 1-14 Bunkyo, Nagasaki 852-8521, Japan*
[3]*Department of Civil Engineering, Monash University, Clayton, Victoria 3800, Australia*

(Received January 15, 2021, Revised March 25, 2021, Accepted April 8, 2021)

Abstract. In this paper, to study the stability of surrounding rock during roadway excavation in different rock mass structures, the physical model test for roadway excavation process in three types of intact rock mass, layered rock mass and massive rock mass were carried out by using the self-developed two-dimensional simulation testing system of complex underground engineering. Firstly, based on the engineering background of a deep mine in eastern China, the similar materials of the most appropriate ratio in line with the similarity theory were tested, compared and determined. Then, the physical models of four different schemes with 1000 mm (height) × 1000 mm (length) × 250 mm (width) were constructed. Finally, the roadway excavation was carried out after applying boundary conditions to the physical model by the simulation testing system. The results indicate that the supporting effect of rockbolts has a great influence on the shallow surrounding rock, and the rock mass structure can affect the overall stability of the surrounding rock. Furthermore, the failure mechanism and bearing capacity of surrounding rock were further discussed from the comparison of stress evolution characteristics, distribution of stress arch, and failure modes in different schemes.

Keywords: physical model; rock mass structure; stress evolution; mechanical bearing characteristic; failure mechanism

1. Introduction

The deformation and failure of surrounding rock mass not only are related to mechanical properties, but also structural features, such as fault, joint, bedding (Bobet 2016, Chen *et al*. 2018, Duan *et al*. 2017, Do *et al*. 2019, Hatzor *et al*. 2015, Ju *et al*. 2020, Jing *et al*. 2021). In the research of rock mass engineering, engineers and scholars often classify rock masses from different perspectives for the convenience (Gholami *et al*. 2013, Potvin *et al*. 2012, Mohammadi *et al*. 2017, Moussaei *et al*. 2019). The structural characteristics of rock mass are important factors affecting the mechanical behavior, deformation and failure forms of rock mass, so the rock mass can be regarded as composed of structural planes and structural bodies. Furthermore, in geotechnical engineering, rock mechanics and engineering geology, rock mass is usually divided into intact rock mass, layered rock mass, blocky rock mass and fractured rock mass according to the structural characteristics of rock mass as shown in Fig. 1. Faults, joints, fissures and other structural planes in the intact rock mass are rare and short, and the rock mass is not cut. In this case, it can be regarded as homogeneous isotropic medium. Layered rock mass, such as sedimentary rock, has roughly parallel structural planes only in one respect and are characterized by significant differences in mechanical properties between parallel and vertical bedding directions. It may be regarded as transversely isotropic medium. The blocky rock mass is cut into regular blocks by several groups of structural planes, while the fractured rock mass is very broken and cut into small pieces of irregular shape due to the dense development of joints and fissures. Because layered and blocky rock masses are affected by discontinuities or structural planes, which expands the discontinuity of rock mass, the overall strength of surrounding rock is reduced, and the mechanical properties are substantially different from that of intact rock mass. Layered rock mass affected by horizontal joints accounts for a large proportion throughout the widest gamut of human activities, and superimposed further by the longitudinal joints, the layered rock mass can be further divided into blocky rock mass. Therefore, it is of great significance to study the deformation and failure characteristics of rock mass with different structures.

In addition, the layered and blocky rock masses are also common in underground excavation engineering especially coal mining, tunnel excavation, water conservancy and hydropower construction. The tunnel or roadway excavation in the deep rock mass inevitably leads to deformation and fracture of the surrounding rock mass of the roadway, which make the surrounding rock mass become a more complex fractured rock mass in structure and mechanical properties. An enormous amount of

*Corresponding author, Professor
E-mail: hongwenjingcumt@126.com
**Corresponding author, Ph.D. Student
E-mail: Y.Gao@monash.edu

ISSN: 2005-307X (Print), 2092-6219 (Online)

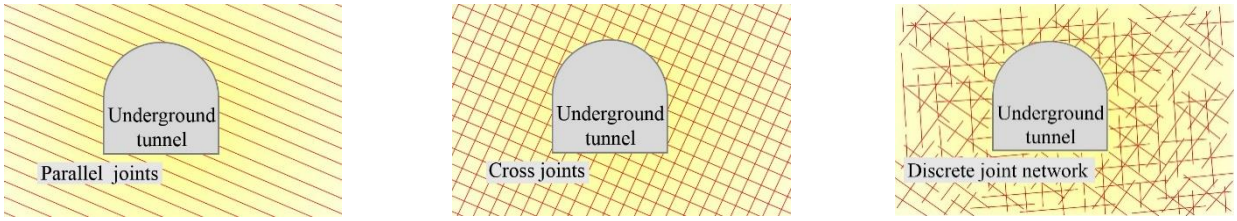

(a) Layered structure (b) Blocky structure (c) Fractured structure

Fig. 1 Surrounding rock mass with different structures

research effort have gone into the stability of surrounding rock mass of excavation engineering (Malkowski 2015, Meng *et al*. 2013, Li *et al*. 2014, Wang *et al*. 2020, Zhang *et al.* 2018). Likewise, there are a large number of discontinuous joints and beddings in the layered and blocky rock masses, which makes the surrounding rock more prone to instability and failure, and its deformation characteristic shows obvious anisotropy, resulting in the mechanical behaviors are very different from those of homogeneous surrounding rock mass (Bewick *et al.* 2019, Chang *et al*. 2018, Ding *et al*. 2019, Jiang *et al*. 2009, Tsesarsky and Hatzor 2006, Roy *et al*. 2018). Therefore, it is necessary to grasp the deformation and failure mechanism of the layered and blocky surrounding rock mass in deep and put forward reliable control methods to ensure the safety of excavation engineering. As two special kinds of engineering rock masses, the mechanical behaviors of layered and blocky rock masses are very important to the overall stability of the engineering, which has become the research object of many scholars. These studies are of great value for understanding the deformation and failure characteristics of the surrounding rock mass in excavation engineering.

Studies and practices have proved that the stability of roadway surrounding rock mass is not only related to the strength of rock mass itself, but also closely related to the surrounding rock structure. However, the experimental studies on the stability of surrounding rock in the process of roadway excavation in complex surrounding rock structure is not in-depth. In this paper, based on the physical and mechanical properties of rock strata in a deep mine in eastern China, first the cement-based rock-like materials with the most appropriate proportion of quartz sand, gypsum and cement were selected, and then the stress evolution processes of surrounding rock mass in the excavation process of rectangular roadway in four types of intact rock mass structures without rockbolt support, intact rock mass structures with rockbolt support, layered rock mass with rockbolt support, and blocky rock mass with rockbolt support were obtained by using the two-dimensional simulation testing system of complex underground engineering independently developed by the State Key Laboratory for Geomechanics and Deep Underground Engineering, China University of Mining and Technology. Furthermore, the failure mechanism and bearing capacity of surrounding rock were further discussed from three aspects of the stress evolution characteristics, stress arch distributions and failure modes in different schemes. This study is of great significance for the stability control of surrounding rock of underground tunnel or tunnel under similar geological conditions.

2. Materials and methods

2.1 Testing system

The physical modeling experiment was carried out by the self-developed underground engineering testing system. The testing system consists of a loading system, computer control system, hydraulic servo control system, and data collection system. Most of the model testing systems are loaded by the way of excavation followed by step increase to designed load, while this testing system adopts the method of the loading first and then excavation. Compared with the actual excavation process of underground engineering, the loading mode of the testing system is more reasonable.

The framework of the test system with the size of 2100 mm (height) × 2100 mm (length) × 600 mm (width) uses cast steel to ensure sufficient rigidity as shown in Fig. 2(a), and its maximum allowable size of physical model is 1000 mm (height) × 1000 mm (length) × 250 mm (width) in Fig. 2(b). The physical model is placed in a vertical pattern, and can be loaded from four directions of top, bottom, left and right. The loading process in each direction is controlled by three oil cylinders. The maximum loading of a single oil cylinder is 300 kN and the stroke is 50 mm. In addition, a transparent acrylic plate with a thickness of 30 mm is installed on the front of the model, which can meet the test requirements for strength, and facilitate the real-time monitoring of deformation and failure of the model by the digital photographic equipment. The back of model is restrained by the lattice steel plate, and a detachable square baffle is reserved in the center to facilitate tunnel excavation.

The whole loading process is controlled by computer control system and hydraulic servo control system. The computer control system can control the loading process according to the loading mode and loading path set before the experiment. The servo control system can independently control the loading of each oil cylinder, and each oil cylinder adopts two oil channels of oil input and output, with the dynamic and static stability accuracy reaching ±2.0 % and ±0.5 % respectively. In the data acquisition system, the static strain test system and various kinds of sensors can be used to obtain the stress evolution of surrounding rock during the test, and the displacement convergence data and failure characteristics of roadway surrounding rock can be

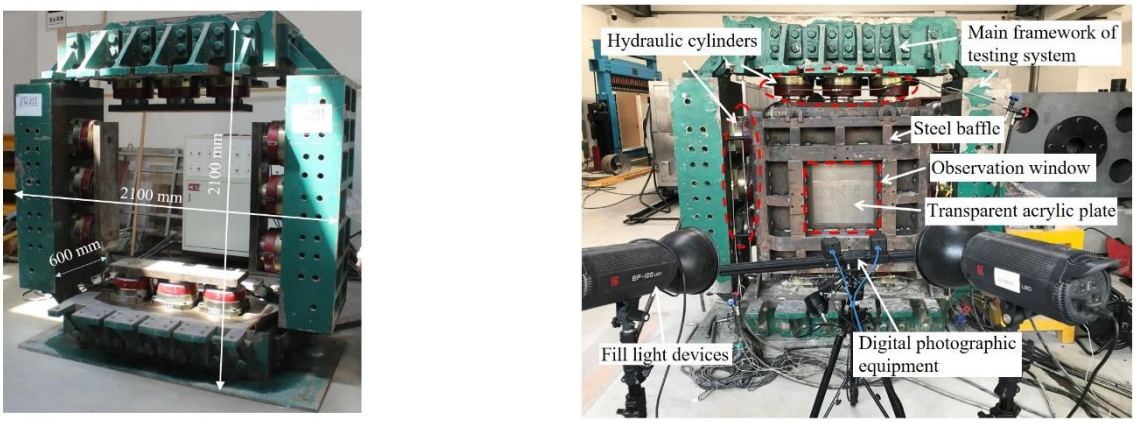

(a) Main framework of testing machine (b) Monitoring system

Fig. 2 Testing system

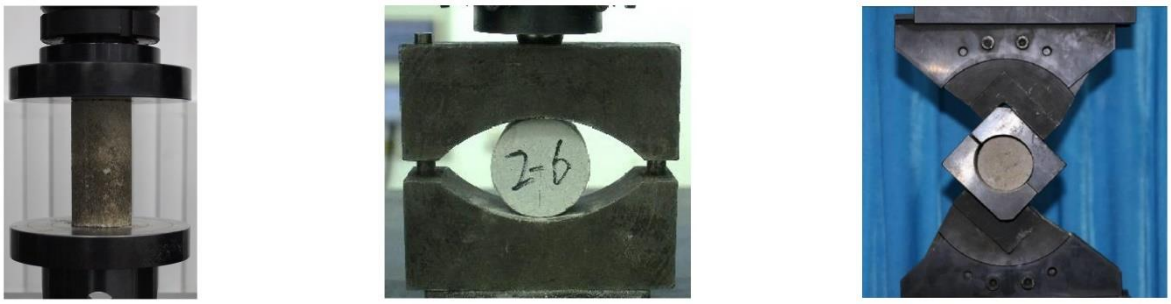

(a) Uniaxial compression test (b) Brazilian disk splitting test (c) Variable angle shear test

Fig. 3 Testing of mechanical properties of similar materials

collected by the digital photographic displacement measurement equipment.

2.2 Materials selection

Taking the rectangular roadway of a deep coal mine in the east of China as the engineering background, the section size of the roadway is 5100 mm (length) × 4200 mm (width), and the buried depth is 742-877 m. The roadway mainly crosses the siltstone stratum, which the physical and mechanical properties are presented in Table 1. To study deformation and failure characteristics of the roadway with surrounding rock mass of different structures in deep rock mass, the similar materials need to be prepared. Based on the mineralogical composition feature of sandstone cemented by mineral particles of various sizes, quartz sand, gypsum and cement are used as similar materials, among which quartz sand is used as aggregate, gypsum and cement as cementitious medium. To obtain the appropriate material ratio matching the physical and mechanical properties of the original siltstone in the engineering site, the similarity ratio should be determined according to the similarity criterion in Eqs. (1)-(3).

$$C_\sigma = C_\gamma C_L \tag{1}$$

$$C_\sigma = C_\varepsilon C_E \tag{2}$$

$$C_u = C_\varepsilon C_E \tag{3}$$

where C_σ is the stress similarity ratio, C_γ is the bulk weight similarity ratio, C_L is the geometric similarity ratio, C_E is the elastic modulus similarity ratio, C_u is the displacement similarity ratio, and C_ε is the strain similarity ratio and C_ε=1 in this paper.

First of all, considering the model size and boundary effect (Jin *et al*. 2018), the geometric similarity ratio was set as C_L =30. According to the geometric similarity ratio, the physical model of 1 m × 1 m × 0.25 m can simulate the engineering site of 30 m × 30 m × 7.5 m. In the same way, the roadway section size of 5100 mm × 4200 mm in the engineering site is scaled down to the rectangular roadway of 170 mm × 140 mm in the physical model. In addition, the bulk weight of a mixture of water, quartz sand, gypsum and cement is about 17.4 kN·m^{-3} and average bulk weight of surrounding rock in site is about 25 kN·m^{-3}, so the bulk weight similarity ratio was set as C_γ =1.44. Furthermore, according to Eqs. (1)-(3), the stress similarity ratio C_σ, elastic modulus similarity ratio C_E and displacement similarity ratio C_u are all 43.2. This provides a basis for determining the proportion of similar materials.

In order to obtain the reasonable similar materials satisfied above similar ratios, twelve proportioning schemes were designed for quartz sand, gypsum, cement and water. The physical and mechanical properties of these mixtures, such as the uniaxial compressive strength, elastic modulus,

Table 1 Physical and mechanical properties of original rock and similar material. UCS indicates the uniaxial compressive strength, E indicates the elastic modulus, σ_t indicates the tensile strength, c indicates the cohesion, φ indicates the internal friction angle, ρ indicates the density

Specimen	UCS (MPa)	σ_t (MPa)	E (GPa)	c (MPa)	ρ (kg·m^{-3})	φ (°)
Sandy mudstone	45.4	6.44	1.89	9.2	2500	32.90
Similar material	0.46	0.16	0.04	0.20	1740	30.68
Actual similarity ratio	98.70	40.25	47.25	46.00	1.44	1.07

Table 2 Surrounding rock structures and anchorage methods of four experimental schemes

Experimental Schemes	Rock mass structures	Joint forms	Supporting modes
One	Intact structure	No joint	No supporting
Two	Intact structure	No joint	Rockbolt supporting
Three	Layered structure	Horizontal joint	Rockbolt supporting
Four	Blocky structure	Horizontal joint and vertical joint	Rockbolt supporting

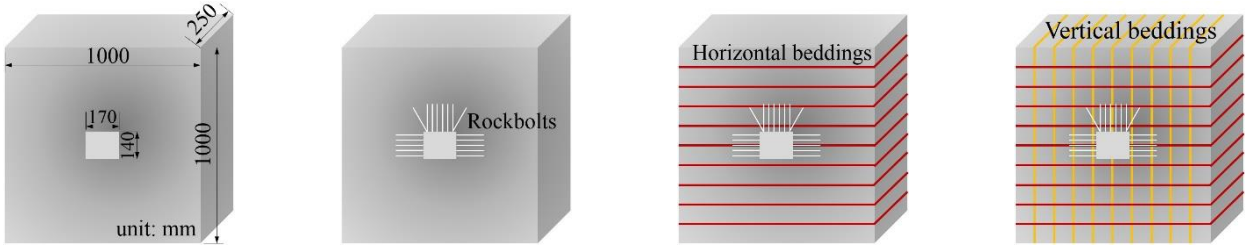

(a) Scheme one (b) Scheme two (c) Scheme three (d) Scheme four

Fig. 4 Diagrammatic sketch of different surrounding rock structure

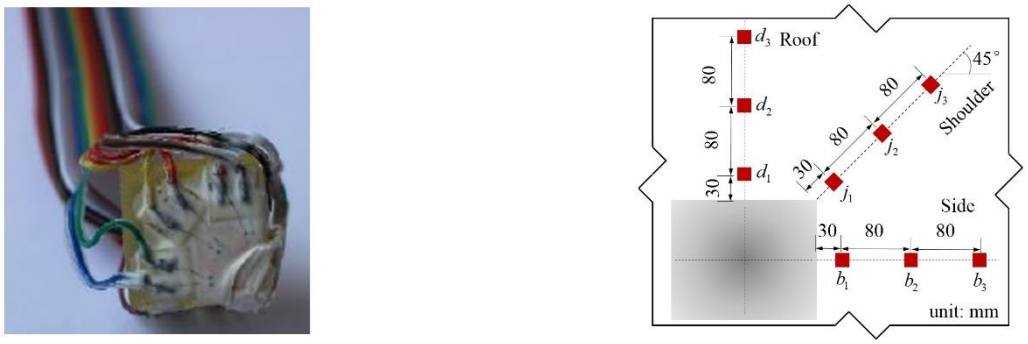

(a) Strainmeter (b) Layout of monitoring points

Fig. 5 Schematic diagram of stress monitoring

tensile strength, cohesion and angle of internal friction, were tested according to the suggestions of ASTM (American Society for Testing and Materials) and ISRM (International Society for Rock Mechanics), as shown in Fig. 3, wherein the uniaxial compressive strength and elastic modulus were measured by uniaxial compression tests, the tensile strength was measured by the Brazilian disk splitting tests, and the cohesion and angle of internal friction were measured by the wedge shear test with variable angle of 45°, 55° and 65°.

Among all the test results, only the similar material with a mass ratio of 60:7:3 for quartz sand, cement and gypsum satisfied those similar ratios, as presented in Table 1. In addition, the vertical stress and horizontal stress of surrounding rock of roadway in site can be obtained in Eqs. (4) and (5).

$$\sigma_V = \gamma H \tag{4}$$

$$\sigma_H = \lambda \sigma_V \tag{5}$$

where σ_H is the vertical stress, σ_V is the horizontal stress, H is the buried depth of the roadway, γ is the bulk weight of surrounding rock mass and λ is the coefficient of horizontal stress.

As mentioned earlier, the buried depth of the roadway in site is 742-877 m, and average bulk weight of surrounding rock mass is about 25 kN·m^{-3}. So according to the maximum buried depth, the vertical and horizontal stresses are 21.93 MPa and 26.28 MPa, respectively. According to

the stress similarity ratio C_σ=43.2, the vertical and horizontal stresses are 0.51 MPa and 0.61 MPa in physical model, respectively. Furthermore, the vertical and horizontal forces applied to the physical model are 127.5 kN and 152.5 kN, respectively. The maximum loading applied by the testing system is 300 kN, and can meet the experimental requirements.

2.3 Experimental scheme

In this study, the effect of the structures of surrounding rock mass on mechanical behaviors of rectangular roadway was mainly considered, so the specific schemes were gave in Fig. 4 and Table 2. In the physical model, the bedding is simulated by mica powder, and the horizontal bedding with spacing of 33 mm and vertical bedding with spacing of 50 mm. In addition, based on the row and line space of the rockbolts of the roof and the side in site is 800 mm × 800 mm, so the row and line space of the similar rockbolts in the physical model is 26.7 mm × 26.7 mm according to geometric similarity ratio. In the preparing process of the model, the rockbolts were embedded and fixed according to the specified position in the experimental scheme. Firstly, the upper, lower, left and right boundaries of the physical model were loaded to the designed stress. Then the roadway was excavated after the stress state of rock mass reached the initial stress equilibrium. In the process of roadway excavation, the stress evolutions of surrounding rock mass were monitored in real time.

Fig. 5(a) gives a kind of self-made strainmeter used to monitor the stress evolution in surrounding rock mass. Considering the symmetry of the physical model, the three monitoring lines were arranged in the roof, shoulder and side of the roadway, and three strainmeters were respectively embedded in each monitoring line as shown in Fig. 5(b). In this paper, it is assumed that the embedded positions of the strainmeters d1, j1 and b1 indicate shallow surrounding rock of the roadway which is 30 mm away from of the roadway wall, the embedded positions of the strainmeters d2, j2 and b2 indicate middle surrounding rock of the roadway which is 110 mm away from of the roadway wall, and the embedded positions of the strainmeters d3, j3 and b3 indicate deep surrounding rock of the roadway which is 190 mm away from of the roadway wall.

The polyurethane cube with side length of 15 mm was adopted as the matrix of the strainmeters, which has high strength and good linear elasticity, and can meet the requirements for stress monitoring. Since the size of the strainmeter is much smaller than the model, it can be approximated that the deformation measured by the strainmeter represents a point in the internal space of the model. Six strain values ε_x, ε_y, ε_z, $\varepsilon^{45^\circ}{}_{xy}$, $\varepsilon^{45^\circ}{}_{xz}$ and $\varepsilon^{45^\circ}{}_{yz}$ in this position can obtained by the strainmeter.

Based on elastic theory, $\varepsilon^{45^\circ}{}_{xy}$ can be written by Eq. (6).

$$\varepsilon_{xy}^{45^\circ} = l^2\varepsilon_x + m^2\varepsilon_y + n^2\varepsilon_z + 2mn\gamma_{yz} + 2nl\gamma_{zx} + 2lm\gamma_{xy} = \frac{1}{2}\varepsilon_x + \frac{1}{2}\varepsilon_y + \gamma_{xy} \quad (6)$$

where l, m and n are the direction cosine of the out-of-plane normal $\vec{n}$.

$$\cos(\vec{n}, x) = l \quad (7)$$

$$\cos(\vec{n}, y) = m \quad (8)$$

$$\cos(\vec{n}, z) = n \quad (9)$$

Likewise, the $\varepsilon^{45^\circ}{}_{yz}$ and $\varepsilon^{45^\circ}{}_{xz}$ also can be written.

$$\varepsilon_{yz}^{45^\circ} = \frac{1}{2}\varepsilon_y + \frac{1}{2}\varepsilon_z + \frac{1}{2}\gamma_{yz} \quad (10)$$

$$\varepsilon_{zx}^{45^\circ} = \frac{1}{2}\varepsilon_x + \frac{1}{2}\varepsilon_z + \frac{1}{2}\gamma_{zx} \quad (11)$$

The shear strain values γ_{xy}, γ_{yz} and γ_{zx} can be written in Eqs. (12)-(14).

$$\gamma_{xy} = 2\varepsilon_{xy}^{45^\circ} - \varepsilon_x - \varepsilon_y \quad (12)$$

$$\gamma_{yz} = 2\varepsilon_{yz}^{45^\circ} - \varepsilon_y - \varepsilon_z \quad (13)$$

$$\gamma_{zx} = 2\varepsilon_{zx}^{45^\circ} - \varepsilon_x - \varepsilon_z \quad (14)$$

Here, six strain values ε_x, ε_y, ε_z, γ_{xy}, γ_{yz} and γ_{zx} can be obtained. Next, according to the six strain values and the relationship between the stress and strain of the polyurethane material of the strainmeter, six stress values in this point can be obtained.

In this paper, the relationship between stress and strain of the polyurethane material used as the matrix of the strainmeters can be expressed in Eq. (15).

$$\sigma = 22.26\varepsilon - 0.0053 \quad (15)$$

It is assumed that the horizontal direction is X-axis, vertical direction is Z-axis and roadway axis is Y-axis, and the physical model is the plane strain model, so the radial stress and tangential stress at any point can be obtained in Eqs. (16) and (17).

$$\sigma_\rho = \sigma_x \cos^2\varphi + \sigma_z \sin^2\varphi + 2\tau_{xz}\sin\varphi\cos\varphi \quad (16)$$

$$\sigma_\varphi = \sigma_x \sin^2\varphi + \sigma_z \cos^2\varphi - 2\tau_{xz}\sin\varphi\cos\varphi \quad (17)$$

Thus, by monitoring the deformation data of strainmeters, the stresses σ_x, σ_y and σ_z of surrounding rock at the location of the embedded strainmeters can be retrieved by Eqs. (6)-(15). Furthermore, the radial stress σ_ρ and tangential stress σ_φ of the roof, shoulder and side were obtained according to Eqs. (16) and (17).

2.4 Physical model preparation

The experimental procedure includes the pouring of physical model, the installation of monitoring equipment, the application of initial stress boundary conditions, roadway excavation and data monitoring. The production of the physical model were shown in Fig. 6. First, calculate the amount of quartz sand, gypsum and cement in each layer, and pour them into the mixer to stir evenly. Then, pour the evenly mixed materials into the frame of the testing

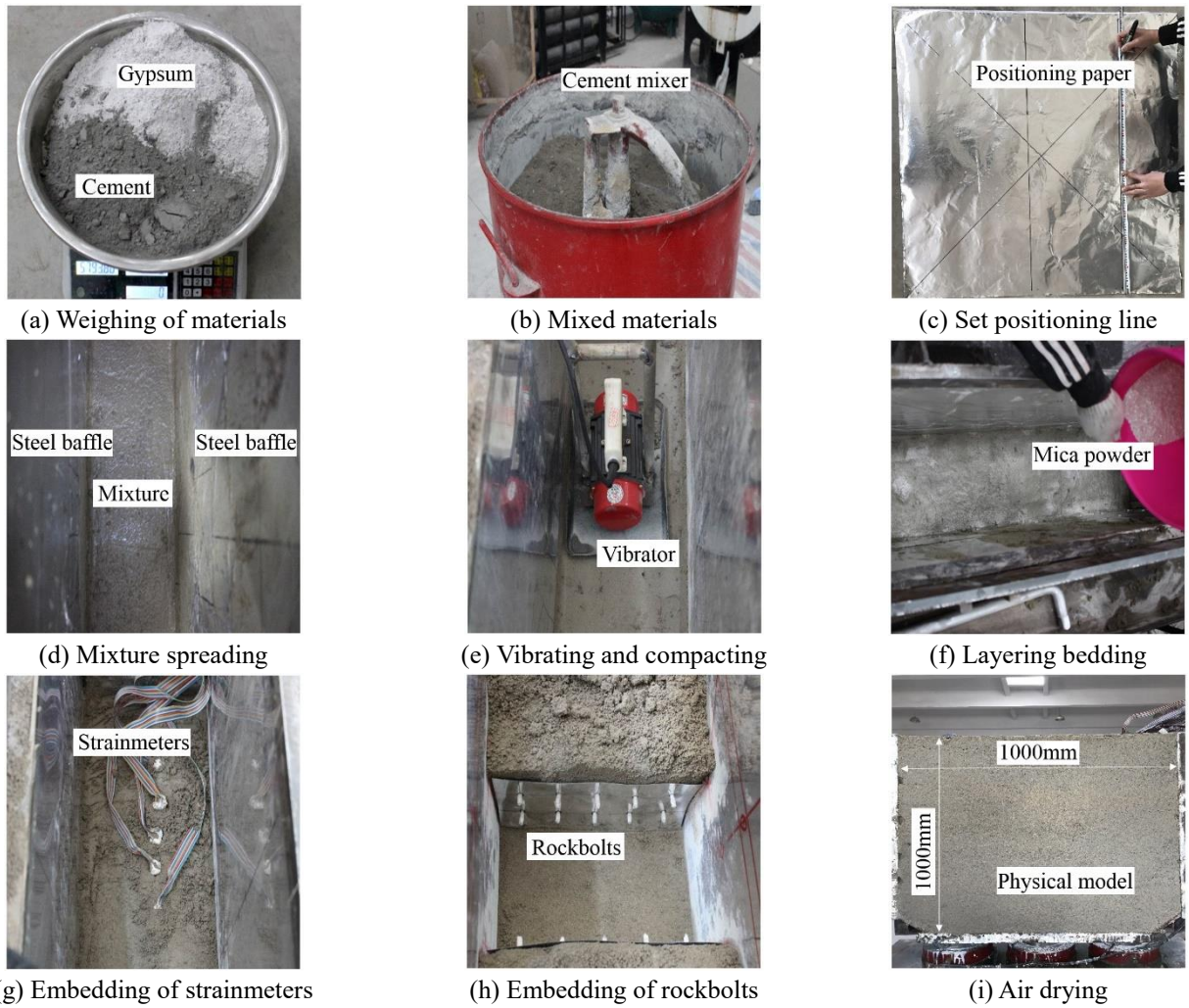

(a) Weighing of materials (b) Mixed materials (c) Set positioning line

(d) Mixture spreading (e) Vibrating and compacting (f) Layering bedding

(g) Embedding of strainmeters (h) Embedding of rockbolts (i) Air drying

Fig. 6 Manufactureing process of physical model

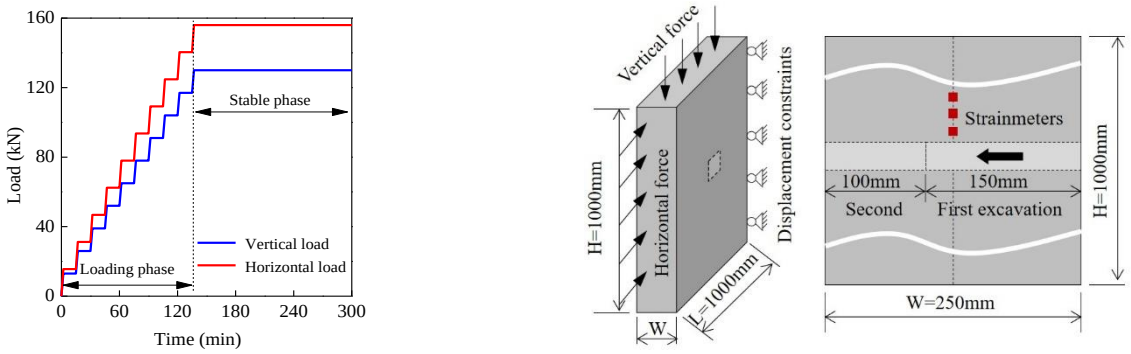

(a) Step loading process before excavation (b) Staged excavation diagram of roadway

Fig. 7 Loading and roadway excavation processes

machine and pave them flat. After being compacted with a hammer, the materials are compacted with a vibrator. Finally, the mica powder is evenly spread on the upper surface to form a bedding. After the completion of the next layer can be laid, so as to achieve the paving of a layer and then ready for the next layer. After the model was completed for about 24 hours, the front and rear baffles of the test bench were removed, and the model was placed for 72 hours to dry under natural conditions.

2.5 Experimental procedure

Before roadway excavation, initial in-situ stress field should be applied to the physical model. In this paper, the loading process was completed in ten times, and the vertical direction load is applied 13 kN each time and the horizontal direction load is 15.6 kN each time as shown in Fig. 7(a). After the initial stress was applied, the roadway was excavated and the excavation process was divided into two

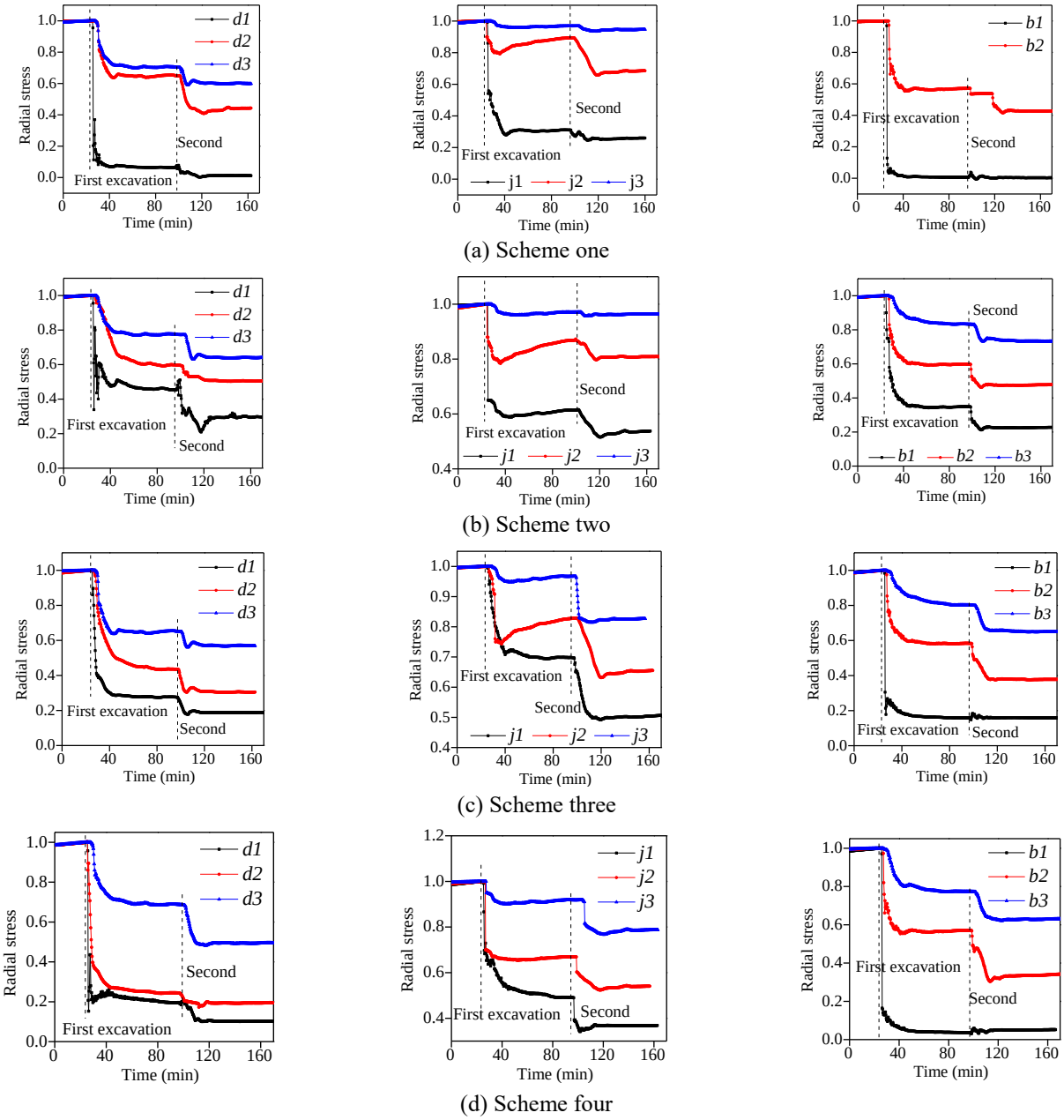

Fig. 8 Evolution process of radial stress

times. After the first excavation, in order to make the embedded strainmeters effectively monitor the stress evolution process of surrounding rock caused by the roadway excavation, the distance of the first excavation should exceed the embedded position of the strainmeters. So the distance of first excavation about 150 mm, and the second time about 100 mm as shown in Fig. 7(b). In the process of roadway excavation, the internal stress of roadway surrounding rock and the surface deformation and failure process were monitored in real time,and the test is completed after the roadway deformation and failure is basically completed.

3. Results and analysis

3.1 Radial stress evolution

For the convenience of comparative analysis, the initial stress of surrounding rock is normalized, and the initial stress before the first excavation is defined as the in-situ stress. The stress after excavation is divided by the in-situ stress value to obtain the radial stress after normalized treatment. It should be noted that in scheme one, the strainmeter j3 embedded in deep rock mass of the side was damaged in the loading process, and the stress data at this position was not detected, which leads to only obtaining the stress evolution data of strainmeters j1, j2 embedded in the shallow and middle rock mass of the side.

The variation of radial stress of surrounding rock relative to the initial stress in different schemes were shown in Fig. 8. It can be seen that the radial stress evolution of surrounding rock in roof, floor, and side of roadway are roughly the same in different schemes. But due to the

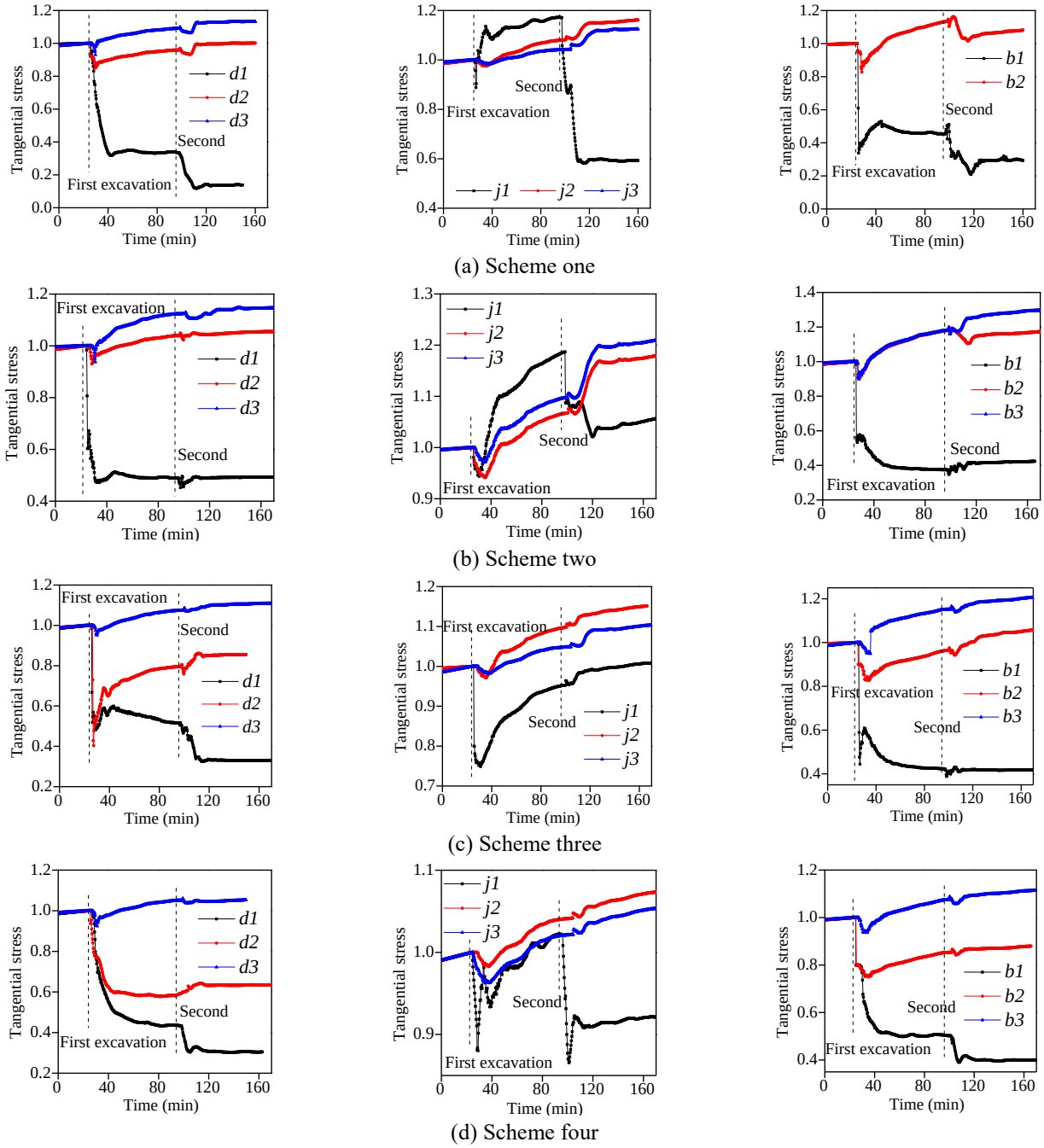

Fig. 9 Evolution process of tangential stress

influence of excavation disturbance, the stress evolution process shows the characteristic of stage change, and the radial stress decreases immediately after roadway excavation, and then tend to be stable. Similarly, magnitude of radial stress after stabilization in the same position of the roadway is significantly different in different schemes due to the influence of bolt support and joints.

3.2 Tangential stress evolution

Same as the normalization of radial stress, the evolution process of tangential stress after normalized treatment is shown in Fig. 9. However, in terms of tangential stress of surrounding rock mass, the evolution process of tangential stress in different schemes is more complicated compared with the evolution process of radial stress.

In scheme one, the stress of the middle and deep rock mass in roof, shoulder and side all show an increasing trend under the influence of excavation disturbances. However, the tangential stress of shallow surrounding rock mass decreases continuously under the influence of two excavation disturbances. Only the tangential stress of shallow rock mass in shoulder rises after the first excavation and then rapidly decreases to 41.7% of the initial stress after the second excavation. In the shallow rock mass of roof and the side, the stable tangential stress is about 15% of the initial stress. In scheme two, stress concentration occurred in the middle and deep rock masses

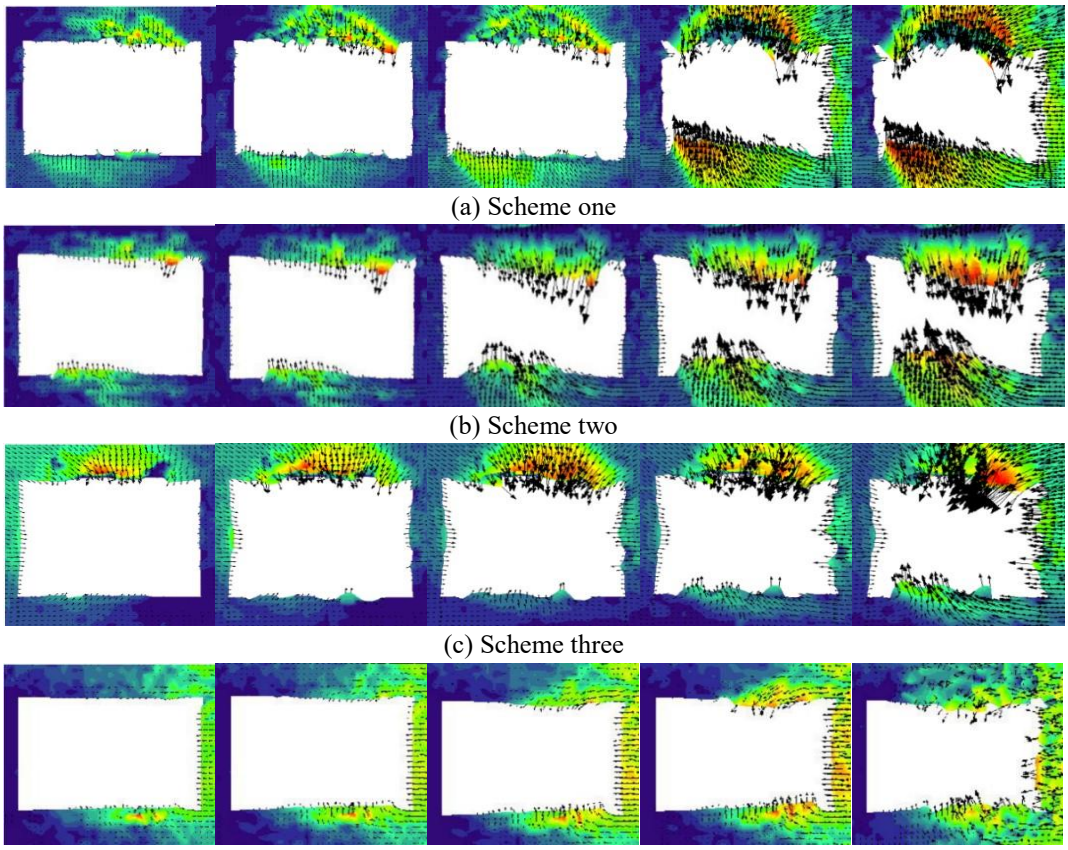

(a) Scheme one

(b) Scheme two

(c) Scheme three

(d) Scheme four

Fig. 10 Displacement vectorgraph of roadway surrounding rock

of the roof and side, and the stress was higher than the initial stress. The degree of stress concentration showed fluctuation after the first and second excavations. However, the shallow rock mass of the roof and top decreases rapidly to about 50.7% and 57.5% of the initial stress due to excavation disturbance. In scheme three, the stress concentration of the deep rock mass at different positions of roadway is more obvious than that of shallow and middle rock masses, and after the second excavation, the stress concentration basically remains at 120% of the initial stress. The stress of the shallow rock mass of the roof and the side decreases continuously during the two times of excavation, but the shallow rock mass of the shoulder increased continuously despite the rapid decrease after the first excavation, and basically stabilized in the original rock stress state after the second excavation. Different from the middle rock masses of shoulder and side, the stress of rock masses in the middle of roof after stabilization is only 82% of the original rock stress. To sum up, the stress fluctuation of tangential stress decreases successively from roof, side to shoulder. In scheme four, the deep surrounding rock mass in the roof of roadway, the middle and deep rock masses of shoulder, and the deep surrounding rock of side show stress concentration phenomenon, which is basically about 110% of the original rock stress. The tangential stress in the shallow and middle rock masses of the roof after stability is 20% and 30% of the initial stress respectively, the tangential stress in the shallow rock mass of the shoulder is 30% of the original rock stress, and the tangential stress in the shallow and middle rock masses is 20% and 30% of the initial stress respectively.

3.3 Deformation and failure process

Fig. 10 show the displacement vectorgraph of roadway surrounding rock with different rock mass structures and the variation process of deformation with time. As we can see from Fig. 10(a) that the roadway surrounding rock shows a large deformation, especially the floor deformation is the most serious. In the early stage after excavation, the roof and floor first show deformation, and the deformation of the roof and floor mainly occurred in the central position of the roadway, while two sides of the roadway almost showed no shrinkage. It can be seen that the roof and floor in the intact rock mass without support are the most sensitive to excavation disturbance, and the side is weak. As time goes on, the sides of the roadway began to shrink along with the deformation of the roof and floor. Finally, the sides began to show rapid deformation, which led to the rapid increase of roof deformation and began to fall off. It can be seen that in the early stage of deformation, the deformation of side surrounding rock lags behind that of roof and floor. With the deformation of roof and floor, the side surrounding rock begins to deform rapidly in the later stage, and the final deformation is greater than the uplift of floor. In addition, although the rock mass is intact, the deformation and failure of the two sides increases the span of the roof, which leads to the roof falling off in the absence of support, and it can

be seen that the deformation and failure of the roof, floor and two sides appear through.

As we can see from Fig. 10(b) that the deformation of surrounding rock is effectively controlled under the bolt support. In the early stage after excavation, the deformation of roadway surrounding rock was mainly dominated by roof and floor, and and the deformations of roof and floor were basically the same, while the two sides show good stability. It can be seen that although the deformation of the roof, floor and sides appeared, the overall deformation was small, especially the deformation of the sides was far less than that of the roof and floor. This is mainly due to the supporting effect of the rockbolt, which makes the roof and the side of the roadway maintain a relatively stable state at the initial stage. As time went on, the deformation of the floor began to intensify. The deformation of the floor began to exceed that of the roof, but the roof did not collapse in a large range. It can be seen that, although the deformation of surrounding rock is effectively controlled in the initial stage after tunnel excavation due to rockbolts supporting, with the rapid increase of floor heave without support, the deformation of roof and sides will still occur.

For layered and blocky rock masses, the deformation and failure process of roadway surrounding rock is obviously different from that of intact rock mass. As we can see from Fig. 10(c) that after excavation, the deformation of roof increases rapidly, while that of floor and two sides increases slowly. It is mainly due to the instantaneous subsidence of the rock mass below the bedding plane of the roof under the horizontal stress compression parallel to the bedding plane. Then the roof subsidence begins to slow down, which is due to the bolt begins to play a supporting role. However, due to the limited supporting effect of the bolt, with the passage of time, the deformation of the roadway in three directions increases rapidly, especially the large-area roof collapse. This is because the adhesion between bedding plane and rock layer is low. After the shallow rock layer of the roof falls, the deep rock layer will collapse continuously under the continuous action of vertical stress. As we can see from Fig. 10d that the floor heave of roadway rises linearly from beginning to end. In the early stage of excavation, the roof subsidence is small due to the anchoring of rockbolts, and it only has a small subsidence after the completion of excavation, and then remains stable. When the bolt gradually fails, the roof subsidence begins to rise rapidly, and the shrinkage of the sides remain basically stable at this stage. With the passage of time, the deformation of roof is basically stable, and the deformation of two sides suddenly increases rapidly. It shows that the each part of the roadway has great relevance due to the action of horizontal and longitudinal joints. The failure of the two sides will aggravate the failure of the roof and floor, and the failure of the floor and roof will in turn affect the failure of the two sides. This coupling relationship makes it necessary to fully consider the effective control of the failure of the two sides when controlling the roof of deep roadway

4. Discussion

4.1 Comparison of stress variation characteristics

To further reveal deformation and failure characteristics of roadway surrounding rock mass with different structures, according to the experimental results in Section 3, the radial stress and tangential stress after stabilization in different schemes are compared.

Fig. 11 gives the radial stress and tangential stress of roof, shoulder and side after stabilization from shallow to deep rock mass in different schemes. As we can see from that for the shallow rock mass, the radial stress after stabilization is in the order of scheme two, scheme three, scheme four and scheme one, and for the middle and deep rock masses, the radial stress after stabilization is in the main order of scheme two, scheme one, scheme three and scheme four. For the shallow rock mass, the tangential stress of roof, shoulder and side in the order of scheme two, scheme three, scheme four and scheme one from the largest to the smallest, and the stress concentration only occurs in the side rock masses of scheme two and scheme three. It can be seen that bolt support can significantly improve the tangential stress of shallow surrounding rock mass. For the middle rock mass, the tangential stress after stabilization is in the order of scheme two, scheme one, scheme three and scheme four from the largest to the smallest. In addition, only scheme one and two show stress concentration in the roof, all scheme all show stress concentration in the side rock mass, and the scheme one, two and three in the floor also have stress concentration. As far as the deep surrounding rock is concerned, all schemes show the phenomenon of tangential stress concentration, and the stress concentration coefficient is about 1.2.

It can be seen that the supporting effect of bolt and the integrity of jointly affect the tangential stress of surrounding rock in the middle and deep rock masses. Generally speaking, the stress evolution process of surrounding rock is staged, but the fluctuation is different under the conditions of different rock mass structure and rockbolt support. Moreover, the different positions of roof, floor and side in the same scheme also show differences. Taking the evolution of radial stress as an example, although the surrounding rock in scheme one is more complete than that in scheme three and four, the influence of excavation disturbance on radial stress in scheme three and four is less than that in scheme one due to the bolt support. Although the same support method is adopted in scheme two, scheme three and scheme four, the integrity of surrounding rock gradually decreases, so the influence of excavation disturbance on radial stress is more and more significant. As for the middle and deep rock masses, although there is no supporting measures in scheme 1, there is little difference in radial stress after stabilization because they are far away from the roadway wall and beyond the scope of bolt support, and due to the influence of the joint, the radial stress in scheme three and scheme four is slightly reduced than that in scheme one and scheme two. It can be seen that with the same anchoring method, the higher the integrity of surrounding rock, the greater the radial stress of surrounding rock after roadway excavation.

4.2 Comparison of arching effect

A large number of engineering practices show that the stress arch is a common form of stress transfer caused by

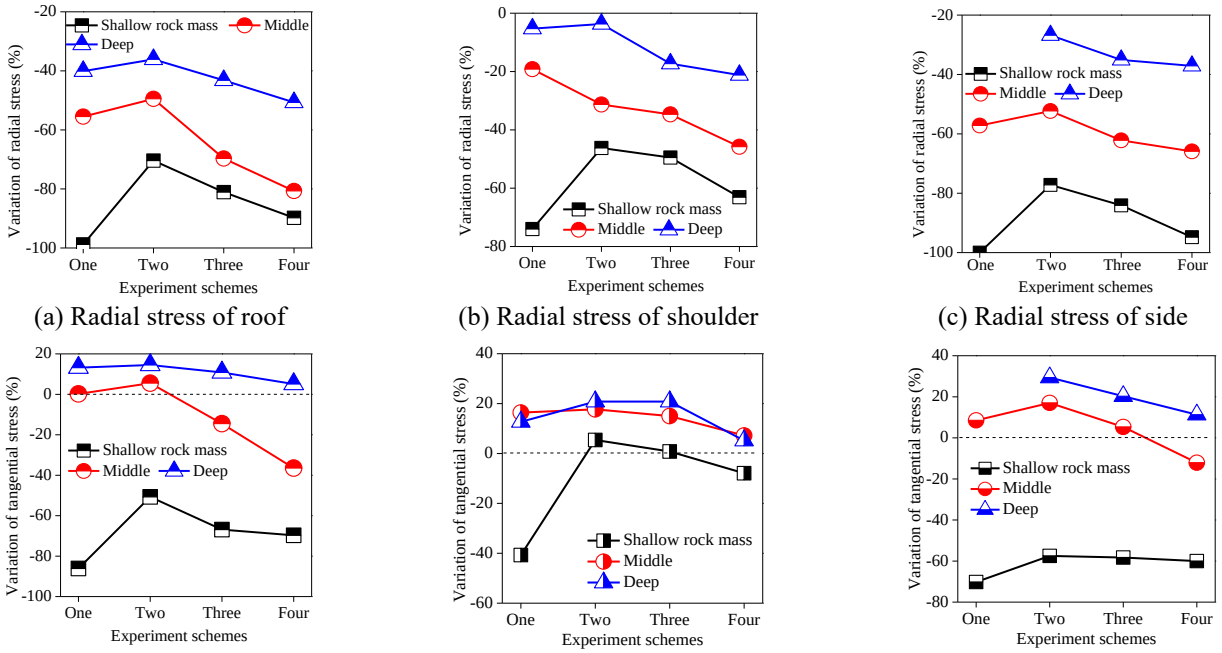

(a) Radial stress of roof (b) Radial stress of shoulder (c) Radial stress of side

(d) Tangential stress of roof (e) Tangential stress of shoulder (f) Tangential stress of side

Fig. 11 The variations of radial stress and tangential stress after stabilization relative to the initial stress

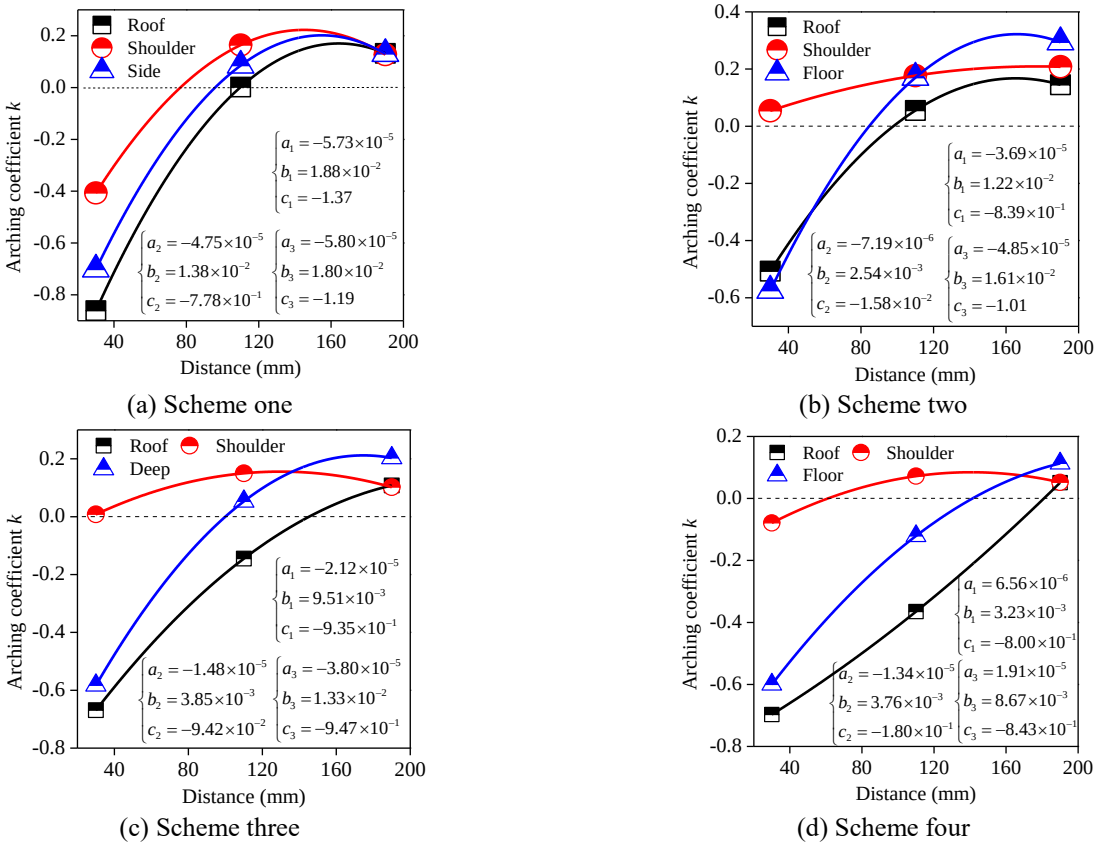

(a) Scheme one (b) Scheme two

(c) Scheme three (d) Scheme four

Fig. 12 Distribution law of arching coefficient versus distances from the roadway wall

underground engineering excavation, which exists not only in circular roadway, but also in the surrounding rock mass of rectangular roadway. In this paper, the bearing capacity of surrounding rock mass can be evaluated according to the arching characteristics of stress arch. Based on the increasing characteristics of tangential stress in the stress arch, the arching coefficient of stress arch is introduced.

$$k = \frac{\sigma_\theta - \sigma_{\theta 0}}{\sigma_{\theta 0}} \tag{18}$$

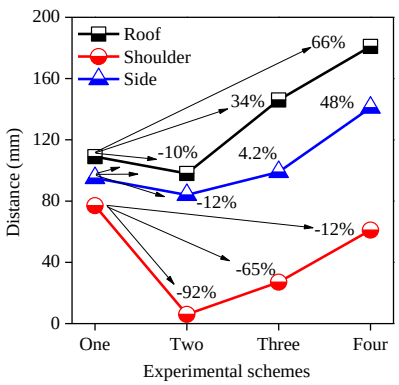

(a) Distance between outer boundary and roadway wall

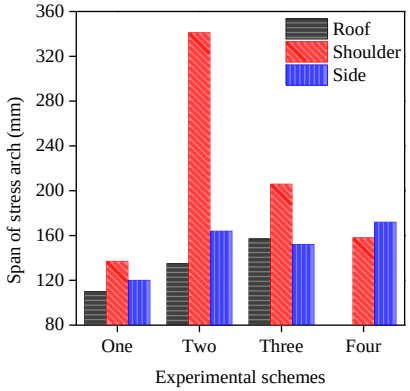

(b) Thickness of stress arch

Fig. 13 Stress arch distribution in different schemes

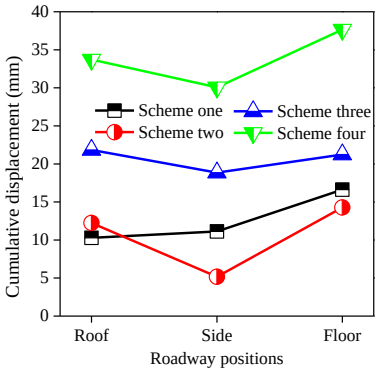

(a) Comparison in different schemes

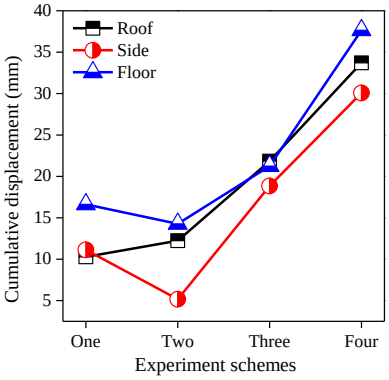

(b) Comparison in different positions of roadway

Fig. 14 Cumulative deformation of roadway surrounding rock

where k is the arching coefficient of stress arch, $\sigma_{\theta 0}$ is the tangential stress of rock mass before excavation, and σ_θ is the tangential stress of rock mass after excavation.

Thus, the inner and outer boundary of the stress arch can be determined according to Eq. (18). When $k > 0$, it indicates that the tangential stress increases, and the rock mass is in the concentration area of tangential stress, which is in the range of stress arch. When $k < 0$, it indicates that the tangential stress decreases, the rock mass is in the stress relief area, and the surrounding rock mass is outside the stress arch. When $k = 0$, it indicates that there is no change in the tangential stress before and after the rock mass excavation, and the location of this point is between the concentration area and the relief area of the tangential stress, or between the concentration area of the tangential stress and the original rock stress area, that is, the inner and outer boundary of the stress arch. Therefore, the arching characteristics of surrounding rock mass can be obtained by analyzing the distribution law of arching coefficient from roadway wall to deep surrounding rock. The tangential stress is selected to calculate the arch coefficient. It should be noted that the tangential stress of the deep surrounding rock mass of the side in scheme one is supplemented, and the stress value is the average value of tangential stresses in deep surrounding rock masses of roof and shoulder.

Fig. 12 gives the distribution law of arching coefficient of surrounding rock versus distances from the roadway wall. It can be seen that the tangential stress increases from the shallow rock mass to the deep rock mass within a certain range of surrounding rock mass. In addition, considering that the deeper rock mass is the original rock stress area, the tangential stress first increases and then decreases to the original rock stress. Similarly, into the same is true of the change of the arching coefficient. The change of arching coefficient should be first increased and then decreased to zero (original rock stress area), and at the distance of roadway walls must be distance exists a peak point. Therefore, it can be quadratic function relation on the arching coefficient of the roof, shoulder and the side with the distance from the roadway walls.

In addition, according to the fitting formula, the distance between the inner and outer boundary of the stress arch and the roadway wall is obtained. It should be noted that the outer boundary of the roof in scheme four is not found. It can be seen that the outer boundary of stress arch not only reflects the tangential stress relief zone, but also reflects the arching ability of roadway surrounding rock. The larger the outer boundary is, the stronger the arching ability is. In addition, the thickness of stress arch also reflects its ability to resist surrounding rock deformation. The thicker the stress arch, the stronger its ability to resist deformation and the less likely it is to fail. Both the outer boundary and the thickness of stress arch reflect the stability of roadway surrounding rock.

Fig. 13 gives the outer boundary and thickness of stress arch in different schemes. It can be seen from Fig. 13(a), under the condition of the same structure of surrounding rock, the arching ability of the shoulder is the strongest, which is obviously higher than that of the side and roof, followed by the side, which is slightly higher than the roof. Under the condition of the different structure of surrounding rock, the arching ability in scheme two is obviously higher than that in other schemes, but the arching ability in scheme one, three and four is also different in different positions of roadway. As far as the shoulder is concerned, the arching ability is weakened in the order of scheme two, scheme three, scheme four and scheme one. As far as roof and side are concerned, the arching ability of scheme two, scheme one, scheme three and scheme four is weakened successively. Distance between outer boundary of stress arch and roadway wall in scheme one reflects the arching ability of surrounding rock when the roadway is excavated in the intact rock mass without support. Compared to scheme one, the arching capacity of roof, shoulder and side is increased by 10%, 92% and 12% respectively in scheme two under the condition of bolting support. It can be seen that the arched ability of surrounding rock is improved by the bolt support, especially the arched ability of shoulder is significantly affected. Under the combined influence of bolt support and horizontal joint (enhanced effect of bolt support, weakened effect of joint) in scheme three, the arch forming capacity of roof and side is reduced by 34% and 4.2% compared to scheme one and the arching capacity of shoulder is increased by 65%. In scheme four, the longitudinal joints were added on the basis of scheme three, and the arching capacity of surrounding rock is further weakened. Similarly, compared to scheme one, arch forming ability of shoulder was only increased by 12%, while arch forming ability of roof and side decreased by 66% and 48% respectively. It can be seen that although there is bolt support, the arch forming capacity is greatly reduced due to the influence of horizontal and vertical joints. It can be seen from the thickness of stress arch in Fig. 13(b) that, except for the larger thickness of the stress arch at the shoulder in scheme two, the thickness of stress arch at different locations of roadway in other schemes is not significantly different. In comparison, the thickness of stress arch in scheme two, scheme three and scheme four is larger than that in scheme one.

Comprehensive comparison of the outer boundary and thickness of stress arch in different schemes shows that the stability of surrounding rock of shoulder under bolt support is effectively controlled by bolt support, while the influence of layered and longitudinal joints on roof and side is higher than that of bolt. By comparing the stability of scheme two, three and four, it can be seen that under the same supporting mode, the more intact the surrounding rocks are, the closer the outer boundary of the stress arch is to the roadway wall. Although there is bolt support in scheme three and four, the outer boundary of stress arch in scheme one is still close to the roadway wall compared to scheme three and four, which shows that bolt support only improves the bearing capacity of shallow surrounding rock, but cannot mobilize the bearing capacity of deep surrounding rock. To sum up, the supporting effect of bolt can significantly improve the bearing capacity of surrounding rock, but rockbolt can only play a limited supporting effect, and the weakening effect of joints still affect the bearing capacity of deep surrounding rock.

4.3 Comparison of deformation and failure characteristics

Furthermore, to reveal the failure mechanism of roadway affected by the bolt support and rock mass structure, combined with the above analysis, it is necessary to further explore failure characteristics of surrounding rock mass in different schemes. The comparison of the cumulative subsidence of the roof, the cumulative heave of floor and cumulative shrink of two sides is shown in Fig. 14.

It can be seen that the deformation presents differences affected by bolt support and rock mass structure, and on the whole, the deformation increases in the order of scheme two, scheme one, scheme three and scheme four. Due to the support effect of bolt, the deformation of the side and the floor in scheme two decreases compared with that in scheme one, while the deformation of the roof increases. Similarly, the deformation in different positions of roadway also shows the characteristics of increasing in the order of scheme two, scheme three and scheme four. When it comes to the side of the roadway, due to the lack of bolt support, the deformation increases by 115.3% in scheme one compared with scheme one, increases by 264.6% in scheme three affected by horizontal joints, and moreover, the deformation decreases by 481.6% in scheme four affected by horizontal and vertical joints. In addition, the cumulative deformation of the roof, floor and side of the roadway is also different in the same scheme. On the whole, the deformation increases in the order of the side, roof and floor of the roadway. In scheme two, the deformation of roof and floor is obviously higher than that of side, increasing by 136.8% and 176.0%, respectively, while the deformation in different positions has little difference in scheme one, three and four.

Fig. 15 shows the characteristics of deformation and failure in different schemes. In scheme one, the surrounding rock of the roof finally spans into an arch without support, and the floor heave also appears. The roof, side and floor of the roadway show the characteristics of shear failure. The stable roadway presents a combination of semicircular arch roof and straight side, as shown in Fig. 15(a). In scheme two, due to the supporting effect of the bolt, although the roof of the roadway sinks, it has not collapsed, which is damaged by mixed shear and tension. The left and right sides also shrank to some extent, but the cracks are not obvious, and the sides were basically intact. However, due to the lack of support measures, the cracks in the roadway floor are seriously developed. The shallow surrounding rock has been separated from the deep surrounding rock, and the floor shows the characteristics of shear failure. Thus, in this case, the excessive floor heave is the main cause of roadway failure. In general, due to bearing structure formed by bolt and surrounding rock, the deformation is not large, the integrity of roadway surrounding rock is relatively

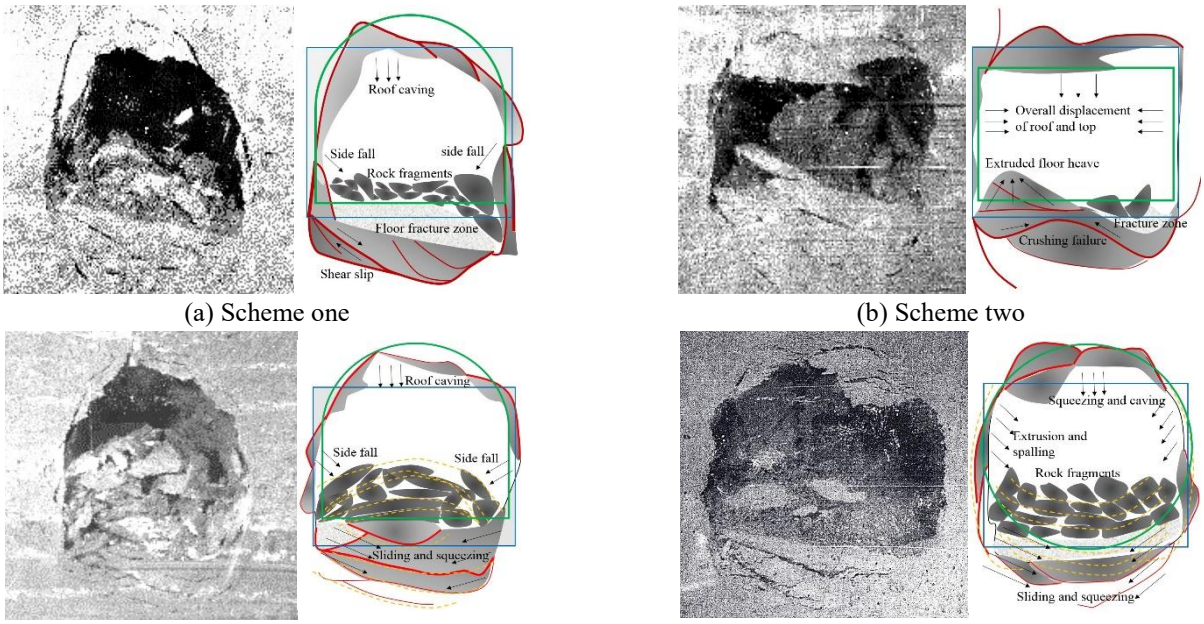

(a) Scheme one (b) Scheme two

(c) Scheme three (d) Scheme four

Fig. 15 Deformation and failure modes of roadway in different schemes

good, and the roadway basically remains rectangular after stabilization, as shown in Fig. 15(b). In scheme three, due to the limited anchoring force of bolts and the low cohesion between layered bedding plane and surrounding rock, it is difficult for the surrounding rock of roof to maintain its own stability. The roof of the roadway is peeled off layer by layer, showing the characteristics of separation and flexural failure. The buckling failure of the floor occurred, accompanied by a certain amount of floor heave. Although the deformation of the two sides was large, it was relatively complete. Finally, a combination supporting structure of semicircular arch roof and straight side is formed, as shown in Fig. 15(c). In scheme four, the roof of the roadway was peeled off layer by layer, which was manifested as separation and flexural failure of roof, shear failure and serious heave of floor, and shear failure of two sides. Under the influence of layered joints, the shallow rock mass of roof tends to be separated from the upper strata at the center line of roadway. However, due to the cutting of longitudinal joints, the surrounding rock of the roof will bend and collapse along the longitudinal joints. In addition, due to a longitudinal joint in the middle of the roadway roof, taking the longitudinal joint as the dividing line, the roadway roof caved in a feature of left-right symmetry, which was finally manifested as a circular section, as shown in Fig. 15(d).

According to the failure characteristics and stress arch distribution law, it can be known that the stability of the rock mass closest to the roadway wall is the worst. The deformation and instability of the roadway can be summarized that when the shallow rock mass is damaged, the deep rock mass changes from three-dimensional stress state to two-dimensional stress state, and the surrounding rock mass reaches equilibrium until the deeper rock mass can no longer meet the failure condition. In addition, the deformation and failure of rock mass in different positions of roadway are correlated. For example, the failure of the rock mass in the side reduce its ability to support the roof, which is equivalent to indirectly increasing the span of the roof. In the case of no support or insufficient support strength and stiffness, the roof will collapse. Furthermore, the joints cut the intact rock mass. Due to the low tensile and shear strength of the joints, the ability of the surrounding rock to resist deformation is weakened, and the rock blocks after cutting are unstable successively, which finally drives the overall instability of surrounding rock.

5. Conclusions

In this paper, the physical models of different rock mass structures (intact structure without rockbolts, intact structure with rockbolts, layered structure with rockbolts, and blocky structure with rockbolts) with the size of 1000 mm (length) × 1000 mm (width) × 250 mm (height) were made. Then, the stress evolution processes of surrounding rock mass were monitored in real time during the roadway excavation by using the self-developed two-dimensional simulation testing system of complex underground engineering and the static strain test system. Furthermore, the bearing capacity of surrounding rock and failure mechanism are further discussed. The main conclusions are as follows:

• The effect of rock mass structure on the bearing capacity of roadway is greater than that of rockbolt support. Although the rockbolts can enhance the bearing capacity of surrounding rock mass, it can only play a role in shallow rock mass due to its limited supporting scope. However, with the decrease of structural integrity of surrounding rock mass, the overall bearing capacity of surrounding rock mass of roadway is weakened.

• The failure modes and instability mechanism of roadway are different due to the effect of the structures of

surrounding rock mass. In addition, the failure of the roadway has a great correlation in different positions, and the failure of the two sides will aggravate the failure of the roof and floor, which in turn will affect the failure of the two sides. Thus different support measures should be taken for different areas of the roadway surrounding rock mass.

• For the roadway with relatively intact rock mass structure, the supporting strength of shallow rock mass should be improved to enhance the ability of anchorage rock structure to resist deformation. For the layered and blocky surrounding rock mass, the lower tensile and shear strength of the bedding plane is the cause of the instability of the surrounding rock mass, the method of rockbolt or anchor cable support combined with grouting should be adopted to strengthen the tensile and shear strength between the rock mass, and make individual blocks form an overall bearing structure to ensure the stability of the surrounding rock mass.

Acknowledgments

This work was supported by National Natural Science Foundation of China (grant number 51734009, 52074259, 51904290). The authors gratefully appreciate these supports. It should be noted that in the process of collating data, the sources of some figures and ideas were not found. I hereby apologize and thank the authorship.

References

Bewick, R.P., Kaiser, P.K. and Amann, E. (2019), "Strength of massive to moderately jointed hard rock masses", *J. Rock Mech. Geotech. Eng.*, **11**(3), 562-575. https://doi.org/10.1016/j.jrmge.2018.10.003.

Bobet, A. (2016), "Deep tunnel in transversely anisotropic rock with groundwater flow", *Rock Mech. Rock Eng.*, **49**(12), 4817-4832. https://doi.org/10.1007/s00603-016-1118-6.

Chang, X., Ma, W.Y., Li, Z.H. and Wang, H. (2018), "Crack behaviour of top layer in layered rocks", *Geomech. Eng.*, **16**(1), 49-58. https://doi.org/10.12989/gae.2018.16.1.049.

Chen, S.J., Qu, X., Yin, D.W., Liu, X.Q., Ma, H.F. and Wang, H.Y. (2018), "Investigation lateral deformation and failure characteristics of strip coal pillar in deep mining", *Geomech. Eng.*, **14**(5), 421-428. https://doi.org/10.12989/gae.2018.14.5.421.

Ding, X.L., Niu, X.Q., Pei, Q.T., Huang, S.L., Zhang, Y.T. and Zhang, C.H. (2019), "Stability of large underground caverns excavated in layered rock masses with steep dip angles: A case study", *B. Eng. Geol. Environ.*, **78**(7), 5101-5133. https://doi.org/10.1007/s10064-018-01440-8.

Do, N.A., Dias, D., Dinh, V.D., Tran, T.T., Dao, V.C., Dao, V.D. and Nguyen P.N. (2019), "Behavior of noncircular tunnels excavated in stratified rock masses-Case of underground coal mines", *J. Rock Mech. Geotech. Eng.*, **11**(1), 99-110. https://doi.org/10.1016/j.jrmge.2018.05.005.

Duan, S.Q., Feng, X.T., Jiang, Q., Liu, G.F., Pei S.F. and Fan, Y.L. (2017), "In situ observation of failure mechanisms controlled by rock masses with weak interlayer zones in large underground cavern excavations under high geostress", *Rock Mech. Rock Eng.*, **46**(9), 2465-2493. https://doi.org/10.1007/s00603-017-1249-4.

Gholami, R., Rasouli, V. and Alimoradi, A. (2013), "Improved RMR rock mass classification using artificial intelligence algorithms", *Rock Mech. Rock Eng.*, **46**(5), 1199-1209. https://doi.org/10.1007/s00603-012-0338-7.

Hatzor, Y.H., Feng, X.T., Li, S.J., Yagoda-Biran, G., Jiang, Q. and Hu, L.X. (2015), "Tunnel reinforcement in columnar jointed basalts: The role of rock mass anisotropy", *Tunn. Undergr. Sp. Tech.*, **46**, 1-11. https://doi.org/10.1016/j.tust.2014.10.008.

Jing, H.W., Yin, Q., Yang, S.Q. and Chen, W.Q. (2021), "Micro-mesoscopic creep damage evolution and failure mechanism of sandy mudstone", *Int. J. Geomech.*, **21**(3), 04021010. https://doi.org/10.1061/(ASCE)GM.1943-5622.0001940.

Jin, C.Y., Shao, A.L., Liu, D., Han, T., Fan, F.Q. and Li, S.G. (2018), "Failure mechanism of highly stressed rock mass during unloading based on the stress arch theory", *Int. J. Geomech.*, **18**(11), 04018146. https://doi.org/10.1061/(ASCE)GM.1943-5622.0001280.

Jiang, Y.J., Li, B. and Yamashita, Y. (2009), "Simulation of cracking near a large underground cavern in a discontinuous rock mass using the expanded distinct element method", *Int. J. Rock Mech. Min. Sci.*, **46**(1), 97-106. https://doi.org/10.1016/j.ijrmms.2008.05.004.

Ju, Y., Ren, Z.Y., Zheng, J.T., Gao, F., Mao, L.T., Chiang, F.P. and Xie, H.P. (2020), "Quantitative visualization methods for continuous evolution of three-dimensional discontinuous structures and stress field in subsurface rock mass induced by excavation and construction-An overview", *Eng. Geol.*, **265**, 105443. https://doi.org/10.1016/j.enggeo.2019.105443.

Li, Y.J., Zhang, D.L., Fang, Q., Yu, Q.C. and Xia, L. (2014) "A physical and numerical investigation of the failure mechanism of weak rocks surrounding tunnels", *Comput. Geotech.*, **61**, 292-307. https://doi.org/10.1016/j.compgeo.2014.05.017.

Malkowski, P. (2015), "The impact of the physical model selection and rock mass stratification on the results of numerical calculations of the state of rock mass deformation around the roadways", *Tunn. Undergr. Sp. Tech.*, **50**, 365-375. https://doi.org/10.1016/j.tust.2015.08.004.

Meng, B., Jing, H.W., Chen, K.F. and Su, H.J. (2013), "Failure mechanism and stability control of a large section of very soft roadway surrounding rock shear slip", *Int. J. Min. Sci. Technol.*, **23**(1), 127-134. https://doi.org/10.3969/j.issn.2095-2686.2013.01.019.

Mohammadi, M., Hossaini, M.F. and Bagloo, H. (2017), "Rock bolt supporting factor: Rock bolting capability of rock mass", *B. Eng. Geol. Environ.*, **76**(1), 231-239. https://doi.org/10.1007/s10064-015-0785-y.

Moussaei, N., Sharifzadeh, M., Sahriar, K. and Khosravi, M.H. (2019), "A new classification of failure mechanisms at tunnels in stratified rock masses through physical and numerical modeling", *Tunn. Undergr. Sp. Tech.*, **91**, 103017. https://doi.org/10.1016/j.tust.2019.103017.

Potvin, Y., Dight, P.M. and Wesseloo, J. (2012), "Some pitfalls and misuses of rock mass classification systems for mine design", *J. S. Afr. I. Min. Metal.*, **112**(8), 697-702.

Roy, N., Sarkar, R. and Bharti, S.D. (2018), "Prediction model for performance evaluation of tunnel excavation in blocky rock mass", *Int. J. Geomech.*, **18**(1), 04017125. https://doi.org/10.1061/(ASCE)GM.1943-5622.0001023.

Tsesarsky, M. and Hatzor, Y.H. (2006), "Tunnel roof deflection in blocky rock masses as a function of joint spacing and friction - A parametric study using discontinuous deformation analysis (DDA)", *Tunn. Undergr. Sp. Tech.*, **21**(1), 29-45. https://doi.org/10.1016/j.tust.2005.05.001.

Wang, E.Y., Chen, G.B., Yang, X.J., Zhang, G.F. and Guo, W.B. (2020), "Study on the failure mechanism for coal roadway stability in jointed rock mass due to the excavation unloading effect", *Energies*, **13**(10), 2515. https://doi.org/10.3390/en13102515.

Zhang, Y.T., Ding, X.L., Huang, S.L., Qin, Y., Li, P. and Li, Y.J. (2018), "Field measurement and numerical simulation of excavation damaged zone in a 2000 m-deep cavern", *Geomech. Eng.*, **16**(4), 399-413. https://doi.org/10.12989/gae.2018.16.4.399.

CC